Multi-low-frequency flexural wave attenuation in Euler-Bernoulli beams using local resonators containing negative-stiffness mechanisms

Jiaxi Zhou[*a], Kai Wang [a], Daolin Xu [a, b], Huajiang Ouyang [c]

[a] *College of Mechanical and Vehicle Engineering, Hunan University, Changsha 410082, PR China,*

[b] *State Key Laboratory of Advanced Design and Manufacturing for Vehicle Body Changsha 410082, PR China,*

[c] *School of Engineering, University of Liverpool, Liverpool L69 3GH, UK*

Abstract

Multi-low-frequency band gaps for flexural waves in beams are realized by using multiple resonators containing negative-stiffness (NS) mechanisms in one unit cell. The resonator is constructed by a vertical spring connecting with two oblique springs, which act as an NS mechanism to counteract the stiffness of the vertical spring, and thus substantially lower the stiffness of the resonator. The band structures of flexural waves in a locally resonant beam are revealed by using the plane wave expansion method, which are validated by numerical simulations. A stop band seamlessly blending attenuation band and complex band is observed, which presents a wide band gap. The band gap can be further broadened by adding more resonators into the unit cell with resonant frequencies surrounding the target frequency by a proper off-set ratio. Finally, an application of this proposed method is demonstrated in attenuating vibrations in a raft beam excited by two forces with different low frequencies, by assigning multi-low-frequency band gaps of receptances at the excitation frequencies.

Keywords: multiple band gaps, low frequency, negative stiffness, local resonance, receptance.

[*] Corresponding author. College of Mechanical and Vehicle Engineering, Hunan University, Changsha 410082, PR China.

E-mail address: jxizhou@hnu.edu.cn (Jiaxi Zhou).

1. Introduction

As well known, waves cannot propagate in periodic structures or materials (also called phononic crystals) in certain frequency ranges, called stop bands or band gaps[1, 2], which can be applied in vibration isolation and wave attenuation at targeted frequencies[3-7]. Due to this fantastic property, in the past several decades, a large amount of research into the theory and applications of phononic crystals has been done, as well documented by Hussein et al.[8].

There are two mechanisms for band gaps, namely, Bragg scattering (BS) and local resonance (LR) mechanisms. It is difficult to achieve a BS band gap at low frequencies, because the centre frequency determined by Bragg scattering condition is inversely proportional to the lattice constant (i.e., dimension of the unit cell). To create a low-frequency BS band gaps, the lattice constant would need to be in very large scale so that it is not practically suitable in many real applications. In contrast, the centre frequency of an LR band gap is independent of the lattice constant, but determined by the resonant frequency of the resonator. Therefore, low-frequency band gaps can be realized by LR mechanisms with lattice constants in wide-ranging scales.

Pioneering work on the LR mechanism was carried out by Liu et al.[2], where the resonator was made from a dense solid core coated by soft materials to open spectral gaps with lattice constants at two orders of magnitude smaller than the relevant wavelength. Wen and his collaborators exhibited the existence of low-frequency band gaps in beams with local resonators by experimental tests[4, 9], and illustrated the band gap behaviour and formation mechanisms[10]. However, the order of magnitude of the centre frequency in most of recent works is a few hundred Hertz. In order to further lower the LR band gap, generally, there are two ways to reduce the resonant frequency, namely, increasing the mass or decreasing the stiffness of a resonator.

In existing LR phononic crystals, mass blocks made from high density materials are generally used, such as Pb[11] and Au[12]. But it is not a wise idea to use a large mass block, due to the size restriction of a unit cell for many practical applications. Recently, Yilmaz et al.[13, 14] proposed a concept of inertial amplification by embedding amplification mechanisms into the unit cell, which can effectively increase the inertial of the resonator, and thus lower the resonant frequency. A prototype of a 2D phononic crystal with inertial amplification mechanisms was fabricated by Acar and Yilmaz[15], and their experimental tests showed wide and deep band gaps at low frequencies. Inspired by this concept, Frandsen et al.[16] studied the wave propagation in a continuous rod attached with periodic amplification mechanisms, which also led to large band gaps at low frequencies. On the other hand, some researchers attempted to lower resonant frequency by reducing the stiffness of a resonator. Bilal and Hussein[17] and Badreddine Assouar et al.[18] punched holes periodically on a host plate, which made solid regions act as springboards of a resonator, resulting in lower band gaps.

However, the above methods might be unworkable to open band gaps at very low frequencies, because it is unrealizable to make the stiffness of a resonator ultra-small, or the mass ultra-large. Therefore, it is still a challenge to realize wave attenuation at extremely low frequencies [8]. As a promising solution to this issue, a local resonator containing negative-stiffness (NS) mechanisms was proposed in our previous work[19] to shift the band gap into very-low-frequency range.

Furthermore, the width of the band gap would become narrow when its centre frequency decreases, as Smith et al. [20] indicated that the edge frequency of the LR band gap is proportional to the resonant frequency. Recently, multiple degrees of freedom (DOF) local resonators were developed to broaden the band gap. Wang et al. proposed a two-DOF resonator [21] and a continuum-beam resonator [22] for attenuating flexural wave in LR beams, and both investigations found wide band gaps. Xiao et al. [23] also proposed multiple periodic arrays of local resonators in one unit cell with distributed resonant frequencies to broaden the band gap, which is known as *rainbow*

trapping[24, 25], named for its ability of splitting propagating waves into a spatial spectrum[26].

Additionally, the tough issues on vibration isolation or wave attenuation at multiple low frequencies are usually encountered in engineering practices[27]. Indeed, more than one band gap can be created in LR phononic crystals by using multi-DOF resonators[28, 29], and the gap also can be tuned by tailoring geometrical dimensions and material properties. But that method[28, 29] does not seems flexible for any combination of target frequencies, due to the restriction on selections of material and structure parameters.

In this paper, multiple resonators containing NS mechanisms in one unit cell are proposed to open multiple band gaps at low target frequencies for flexural wave attenuation in Euler-Bernoulli beams. The resonator consists of one vertical spring and two oblique springs, which are utilized as an NS mechanism to counteract the positive stiffness of the vertical spring[30]. The net stiffness of the resonator can be tuned to be very low by the NS mechanisms, which has been verified in our previous work[19]. The band structures for multiple target frequencies are calculated by using plane wave expansion (PWE) method when damping is taken into account, which are also validated by numerical simulations. Inspired by Xiao et al. [23], more resonators with natural frequencies surrounding the target frequencies are added into the unit cell to broaden the band gaps, especially for very low target frequencies. Finally, to demonstrate an application of this proposed method, vibration attenuations of a raft beam excited by two separate forces with different low frequencies are carried out by assigning two band gaps of receptances at these exciting frequencies.

2. Model and methods of calculation

Consider an Euler-Bernoulli beam periodically attached with local resonators containing NS mechanisms, as shown in Fig. 1. There are *N* resonators in one unit cell

installed at an equal interval, and each resonator has the same mass m_r, but different stiffness, which can be designed to be very low by the counteraction from NS mechanisms. To filter out waves at multiple undesired low frequencies, called target frequencies here, the stiffnesses of those resonators in the unit cell are tuned to create band gaps at these target frequencies.

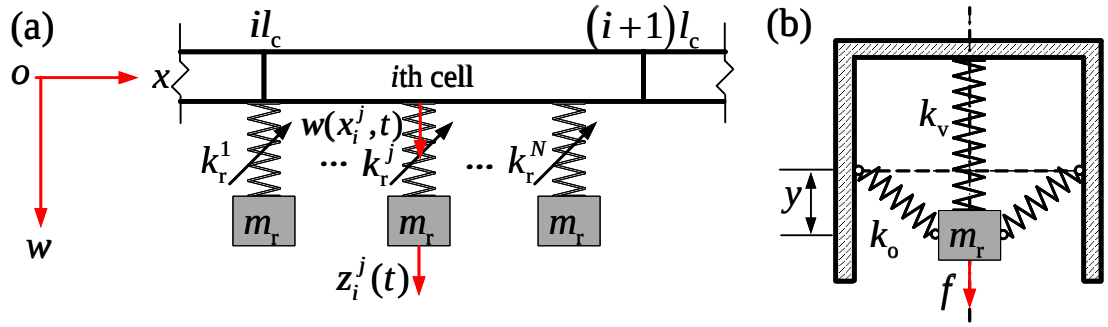

Fig. 1 Schematic diagrams of (a) the LR beam and (b) the resonator.

The resonator is comprised of two oblique springs, a vertical spring and a mass, as shown in Fig. 1b. Two oblique springs provide a negative stiffness in the vertical direction when the mass oscillates around the equilibrium position, which is utilized to counteract the positive stiffness of the vertical spring. It is worth noting that the capability of suspending heavy mass is not reduced, because the mass is completely suspended by the vertical springs at the static equilibrium, at which point the oblique springs are perpendicular to the vertical one. It is assumed that the mass oscillates only along the vertical direction, and the oblique springs deform symmetrically with respect to the vertical spring.

Although the static analysis of the resonator has been done in our previous work[19], the restoring force and stiffness of the resonator as functions of the displacement y are given here for the sake of completeness,

$$f = k_v\left[1-(1-\eta)\frac{(l-\Delta l)}{\Delta l}\left(\frac{l}{\sqrt{(l-\delta)^2+y^2}}-1\right)\right]y \tag{1}$$

$$k = k_{\mathrm{v}}\left[1-\left(1-\eta\right)\frac{\left(l-\Delta l\right)}{\Delta l}\left(\frac{l\left(l-\Delta l\right)^{2}}{\left[\left(l-\Delta l\right)^{2}+y^{2}\right]^{\frac{3}{2}}}-1\right)\right] \tag{2}$$

where k_{v} is the stiffness of the vertical spring, l is the original length of the oblique spring, Δl is the pre-compression of the oblique spring at the static equilibrium, and η $(0 \le \eta \le 1)$ denotes the ratio of the targeted net stiffness of the resonator at the static equilibrium position to k_{v}. The stiffness of the resonator can be successfully reduced from k_{v} to ηk_{v} at the static equilibrium by the neutralization from NS mechanisms, subjected to the following condition

$$\frac{k_{\mathrm{o}}}{k_{\mathrm{v}}} = \frac{\left(1-\eta\right)\left(l-\Delta l\right)}{2\Delta l} \tag{3}$$

where k_{o} is the stiffness of the oblique spring.

Note that, the stiffness of the resonator is equal to ηk_{v} only at the static equilibrium, while it will increase as the mass deviates from this position, or in other words, it is nonlinear. To degrade the degree of nonlinearity in the vicinity of the static equilibrium, the displacement range corresponding to the stiffness smaller than k_{v}, $y_{\mathrm{d}} = \sqrt{l^{\frac{2}{3}}\left(l-\Delta l\right)^{\frac{4}{3}}-\left(l-\Delta l\right)^{2}}$, is maximized, and one can easily obtain its solution as $\Delta l_{\mathrm{opt}} = \left[1-\left(2/3\right)^{3/2}\right]l$. In practice, the pre-compression Δl is easy to be adjusted by controlling the pitch of the oblique spring screwed into the connecter, which also can be used to guarantee the counteracting stiffness with the ratio of $1-\eta$ against possible manufacturing errors of the springs.

2.1 Plane wave expansion (PWE) method

The transfer matrix (TM) method[9, 31-36] is unable to take damping of the beam and resonators into account, but the PWE method[23, 37-42] with the form of $q\left(\omega\right)$ can

predict the band structures considering damping in both the host structure and resonators. Although the resonator has a typical feature of nonlinear stiffness (Eq. (2)), the linearized stiffness at the static equilibrium is adopted to calculate the propagation constant using the PWE method, under the assumption that the resonator undergoes small-amplitude oscillations.

The equation of motion of the LR beam with structural damping is given by

$$\begin{aligned} &E\left(1+\chi_{\mathrm{b}}\sqrt{-1}\right)I\frac{\partial^4 w}{\partial x^4}+\rho A\frac{\partial^2 w}{\partial t^2}=\sum_{i=-\infty}^{\infty}\sum_{j=1}^{N} f\left(x_i^j,t\right)\delta\left(x-x_i^j\right) \\ &f\left(x_i^j,t\right)=\eta_j k_{\mathrm{v}}\left(1+\chi_{\mathrm{r}}\sqrt{-1}\right)\left[z_i^j\left(t\right)-w\left(x_i^j,t\right)\right] \end{aligned} \tag{4}$$

where χ_{b} and χ_{r} are the loss factors of the beam and the resonator, respectively, $\delta\left(x\right)$ is the Dirac function, and $x_i^j=il_c+\left(j-1\right)l_c/N$. l_c is the lattice constant, $w\left(x,t\right)$ is the transverse deflection of the beam, and $z_i^j\left(t\right)$ is the absolute displacement of the *j*th resonator in the *i*th unit cell. All the resonators are assumed to have the same damping. Considering the periodicity of the beam, the displacement can be expanded by

$$w\left(x,t\right)=\sum_{s=-\infty}^{\infty}W_s e^{-\sqrt{-1}\left(q+2s\pi/l_c\right)x}e^{\sqrt{-1}\omega t} \tag{5}$$

where q is the Bloch wave vector, appearing in the form of a scalar for one-dimension wave propagation. Substituting Eq. (5) into Eq. (4), one can obtain

$$\begin{aligned} &\sum_{s=-\infty}^{\infty}\left[E\left(1+\chi_{\mathrm{b}}\sqrt{-1}\right)I\left(q+2s\pi/l_c\right)^4-\rho A\omega^2\right]W_s e^{-\sqrt{-1}\left(q+2s\pi/l_c\right)x} \\ &=\sum_{i=-\infty}^{\infty}\sum_{j=1}^{N}\sum_{s=-\infty}^{\infty}\tilde{K}_j W_{\bar{s}} e^{-\sqrt{-1}\left(q+2\bar{s}\pi/l_c\right)x_i^j}\delta\left(x-x_i^j\right) \\ &=\sum_{i=-\infty}^{\infty}\sum_{j=1}^{N}\sum_{s=-\infty}^{\infty}\tilde{K}_j W_{\bar{s}} e^{-\sqrt{-1}\left(q+2\bar{s}\pi/l_c\right)\left(j-1\right)l_c/N}e^{-\sqrt{-1}qil_c}\delta\left[x-il_c-\left(j-1\right)l_c/N\right] \end{aligned} \tag{6}$$

where

$$\tilde{K}_j=\frac{\eta_j k_{\mathrm{v}}\left(1+\chi_{\mathrm{r}}\sqrt{-1}\right)m_{\mathrm{r}}\omega^2}{\eta_j k_{\mathrm{v}}\left(1+\chi_{\mathrm{r}}\sqrt{-1}\right)-m_{\mathrm{r}}\omega^2} \tag{7}$$

Due to the properties of Dirac function, one can achieve the following expression

$$\begin{aligned}
&\sum_{i=-\infty}^{\infty} e^{-\sqrt{-1}qil_c}\delta\left[x-il_c-\left(j-1\right)l_c/N\right] \\
&= e^{-\sqrt{-1}q\left[x-\left(j-1\right)l_c/N\right]}\sum_{i=-\infty}^{\infty}\delta\left[x-il_c-\left(j-1\right)l_c/N\right] \\
&= e^{-\sqrt{-1}q\left[x-\left(j-1\right)l_c/N\right]}\frac{1}{l_c}\sum_{s=-\infty}^{\infty} e^{\sqrt{-1}(2s\pi/l_c)(j-1)l_c/N}e^{-\sqrt{-1}(2s\pi/l_c)x}
\end{aligned} \tag{8}$$

Substituting Eq. (8) into Eq. (6) yields

$$\begin{aligned}
&l_c\left[E\left(1+\chi_{\mathrm{b}}\sqrt{-1}\right)I\left(q+2s\pi/l_c\right)^4-\rho A\omega^2\right]W_s \\
&=\sum_{j=1}^{N}\sum_{\bar{s}=-\infty}^{\infty}\tilde{K}_j W_{\bar{s}} e^{-\sqrt{-1}(2\bar{s}\pi/l_c)(j-1)l_c/N}e^{\sqrt{-1}(2s\pi/l_c)(j-1)l_c/N}
\end{aligned} \tag{9}$$

By truncating the infinite series, Eq. (9) can be rewritten in a matrix form,

$$\left(\bar{q}^4\mathbf{I}+\bar{q}^3\mathbf{A}_3+\bar{q}^2\mathbf{A}_2+\bar{q}\mathbf{A}_1+\mathbf{A}_0\right)\mathbf{W}=\mathbf{0} \tag{10}$$

where $\bar{q}=ql_c$, $\mathbf{W}=\left\{W_{-S},W_{-S+1},\cdots W_S\right\}^{\mathrm{T}}$, $(2S+1)$ is the number of the kept terms in the series expansion, $\mathbf{I}$ and $\mathbf{0}$ are identity and zero matrices with $\left(2S+1\right)\times\left(2S+1\right)$ dimension, respectively, and

$$\begin{aligned}
\mathbf{A}_0 &= \mathrm{diag}\left[16\pi^4\left(-S\right)^4 \quad 16\pi^4\left(-S+1\right)^4 \quad \cdots \quad 16\pi^4S^4\right] \\
&\quad -\frac{\rho A\omega^2 l_c^4}{E\left(1+\chi_{\mathrm{b}}\sqrt{-1}\right)I}\mathbf{I}-\frac{l_c^3}{E\left(1+\chi_{\mathrm{b}}\sqrt{-1}\right)I}\mathbf{K} \\
\mathbf{A}_1 &= \mathrm{diag}\left[32\pi^3\left(-S\right)^3 \quad 32\pi^3\left(-S+1\right)^3 \quad \cdots \quad 32\pi^3S^3\right] \\
\mathbf{A}_2 &= \mathrm{diag}\left[24\pi^2\left(-S\right)^2 \quad 24\pi^2\left(-S+1\right)^2 \quad \cdots \quad 24\pi^2S^2\right] \\
\mathbf{A}_3 &= \mathrm{diag}\left[8\pi\left(-S\right) \quad 8\pi\left(-S+1\right) \quad \cdots \quad 8\pi S\right]
\end{aligned} \tag{11}$$

where

$$\begin{aligned}
&\mathbf{K}=\sum_{j=1}^{N}\tilde{K}_j\mathbf{f}_j\mathbf{g}_j \\
&\mathbf{f}_j=\left\{e^{\sqrt{-1}(-2S\pi/l_c)(j-1)l_c/N} \quad e^{\sqrt{-1}(-2(S-1)\pi/l_c)(j-1)l_c/N} \quad \cdots \quad e^{\sqrt{-1}(2S\pi/l_c)(j-1)l_c/N}\right\}^{\mathrm{T}} \\
&\mathbf{g}_j=\left\{e^{-\sqrt{-1}(-2S\pi/l_c)(j-1)l_c/N} \quad e^{-\sqrt{-1}(-2(S-1)\pi/l_c)(j-1)l_c/N} \quad \cdots \quad e^{-\sqrt{-1}(2S\pi/l_c)(j-1)l_c/N}\right\}
\end{aligned} \tag{12}$$

For a given ω, one can obtain $8S+4$ solutions for q from the eigenvalue

equation, i.e., Eq. (10). The lowest component, whose real part lies inside the first Brillouin zone, is considered to be the most accurate solution[23], and thus it is adopted to demonstrate the band structure. Note that only the solution of the travelling wave is utilized to show the band structure, and the evanescent wave (with zero real part) is not presented here.

2.2 Dynamic analysis of the LR beam with finite length

In order to verify the band structure revealed by the PWE method, the equations of motion of the beam coupled with the proposed resonators are solved by using the Galerkin method. Note that the actual nonlinear stiffness of the resonator (i. e., Eq. (2)) is used here rather than the linearized one. Further, the band structure is demonstrated by vibration transmittance, which is defined by a ratio of the displacement amplitude of output signal (at the right-hand end of the beam) to that of the input signal (at the left-hand end).

When only the damping in the resonator is considered, the equations of motion of the LR beam and resonators can be written as

$$EI\frac{\partial^4 w}{\partial x^4}+\rho A\frac{\partial^2 w}{\partial t^2}=f_{\mathrm{R}}(t)\delta(x-0)+\sum_{i=1}^{n}\sum_{j=1}^{N}f\left(x_i^j,t\right)\delta\left(x-x_i^j\right) \tag{13}$$

$$m_{\mathrm{r}}\ddot{z}_i^j(t)+f_{\mathrm{d}}\left(x_i^j,t\right)+f\left(x_i^j,t\right)=0,\quad i=1\sim n,\ j=1\sim N \tag{14}$$

where $f_{\mathrm{R}}(t)$ is a random excitation within a bandwidth from 1 to 400 Hz, which acts at the left-hand end of the beam. $f_{\mathrm{d}}\left(x_i^j,t\right)$ and $f\left(x_i^j,t\right)$ are the damping and restoring forces between the resonator and the beam, respectively, which are given by

$$f_{\mathrm{d}}\left(x_i^j,t\right)=c\left[\dot{z}_i^j(t)-\dot{w}\left(x_i^j,t\right)\right] \tag{15}$$

$$\begin{aligned}f\left(x_i^j,t\right)=k_{\mathrm{v}}\left[z_i^j(t)-w\left(x_i^j,t\right)\right]&\frac{-b\pm\sqrt{b^2-4ac}}{2a}\\&\times\left\{1-(1-\eta)\frac{\bar{a}}{1-\bar{a}}\left(\left(\bar{a}^2+\left[z_i^j(t)-w\left(x_i^j,t\right)\right]^2/l^2\right)^{-\frac{1}{2}}-1\right)\right\}\end{aligned} \tag{16}$$

where $c = 2\zeta\sqrt{m_{\mathrm{r}}k_{\mathrm{v}}}$ is the damping coefficient for all the resonators.

The Galerkin method is utilized to discretize the system, and thus $w(x,t)$ can be assumed to be

$$w(x,t)=\sum_{p=1}^{P}\phi_p(x)Q_p(t) \tag{17}$$

where $\phi_p(x)$ and $Q_p(t)$ are the *p*th trail function and generalized displacement, respectively. By substituting Eq. (17) into Eq. (13), and then multiplying the resultant equation by the weight functions $\varphi_p(x)$ and integrating it from 0 to *L*, one can obtain

$$\begin{aligned} &EI\sum_{p=1}^{P}\int_0^L \phi_p^{(4)}(x)\varphi_p(x)\mathrm{d}xQ_p(t)+\rho A\sum_{p=1}^{P}\int_0^L \phi_p(x)\varphi_p(x)\mathrm{d}x\ddot{Q}_p(t)\\ &\quad=\int_0^L \varphi_p(x)\delta(x-0)\mathrm{d}x f_{\mathrm{R}}(t)+\sum_{i=1}^{n}\sum_{j=1}^{N}\int_0^L \varphi_p(x)\delta\left(x-x_i^j\right)\mathrm{d}x f\left(x_i^j,t\right)\end{aligned} \tag{18}$$

where the superscript (4) denotes the forth partial derivative with respect to *x*.

Both $\phi_p(x)$ and $\varphi_p(x)$ are selected as the mode function $\phi_p(x)$ of the Euler-Bernoulli beam with free-free end boundary condition, i.e.

$$\begin{aligned}\phi_p(x)&=\sin(\beta_p x)+\sinh(\beta_p x)\\ &\quad+\frac{\sin(\beta_p L)-\sinh(\beta_p L)}{\cosh(\beta_p L)-\cos(\beta_p L)}\left[\cos(\beta_p x)+\cosh(\beta_p x)\right]\end{aligned} \tag{19}$$

where $\cos(\beta_p L)\cosh(\beta_p L)=1$, $L=nl_{\mathrm{c}}$ is the length of the beam.

Considering the orthogonality of mode functions, Eq. (18) can be rewritten as

$$\begin{aligned}&m_p\ddot{Q}_p+c_p\dot{Q}_p+k_pQ_p\\ &=\phi_p(0)\,f_{\mathrm{R}}(t)+\sum_{i=1}^{n}\sum_{j}^{N}\phi_p\left(x_i^j\right)f_{\mathrm{d}}\left(x_i^j,t\right)+\sum_{i=1}^{n}\sum_{j}^{N}\phi_j\left(x_i^j\right)f\left(x_i^j,t\right)\end{aligned} \tag{20}$$

where $m_p=\rho A\int_0^L \phi_p^2(x)\mathrm{d}x$, $k_p=EI\int_0^L \phi_p^{(4)}(x)\phi_p(x)\mathrm{d}x$.

The displacements in generalized coordinates of the beam and the absolute displacements of all oscillators can be directly obtained by solving simultaneous equations (20) and (14), and then substituting these generalized displacements into Eq. (17) gives the displacement responses of the beam. Note that the number of Galerkin truncation P should be large enough to meet the requirement on computational accuracy.

3. Numerical experiments

In this section, numerical examples are analysed to demonstrate how to open multiple band gaps at target low frequencies by using the proposed multiple resonators. To further broaden bandwidths of the band gaps, several resonators with resonant frequencies surrounding the target frequencies are added into the unit cell. How far away the natural frequency of the added resonator should deviate from the target frequency is also discussed. Finally, the application of this proposed method in multi-low-frequency vibration attenuations of a raft beam is demonstrated.

3.1 Multi-low-frequency band gaps

3.1.1 Band gaps predicted by PWE

Consider a beam with the following parameters: density ρ=2700 kg/m^3, sectional area A=4×10^{-5} m^2, flexural rigidity EI=0.9333 Nm^2, length of the unit cell (lattice constant) l_c=0.1 m. For the resonators, the mass ratio (total mass of the resonators to that of the beam segment in the unit cell) is μ=0.5, and each resonator has the same mass $m_{\mathrm{r}} = \mu\rho A l_c / N$. The stiffness of the resonator is determined by the central frequency of the band gap at which the flexural wave is designed to be attenuated.

For example, the flexural waves at frequencies $\omega_o/3$, $2\omega_o/3$, and ω_o ($\omega_o/2\pi=200\,\mathrm{Hz}$) are designated to be attenuated simultaneously, and thus the corresponding stiffness of three resonators (*N*=3) in the unit cell should be designed as $k_v/9$, $4k_v/9$, and k_v ($k_v=m\omega_o^2$), namely, the ratios of the net stiffness (i.e., the linearized stiffness of the resonator) are $\boldsymbol{\eta}=\{\eta_1,\eta_2,\eta_3\}=\{1/9,4/9,1\}$. According to Eq. (3), i.e., $k_o/k_v=(1-\eta)(l-\Delta l)/2\Delta l$, and $\Delta l_{opt}=\left[1-(2/3)^{3/2}\right]l$, the stiffness of the oblique spring can be determined by $k_{o,j}=0.5973(1-\eta_j)k_v$. In other words, the stiffness of the resonator can be easily tuned to a desired value by adjusting only the oblique stiffness.

The band structures of flexural wave propagation in this LR beam obtained by using PWE method are depicted in Fig. 2, when no damping is considered. In this figure, only the solutions of travelling wave are shown, and those of evanescent wave are not depicted. The real part of the solution and the imaginary one are demonstrated in Fig. 2a and Fig. 2b, respectively. The solution by using the PWE method is denoted by dashed lines, which is verified by the TM method[9, 19], as represented by the solid lines. Obviously, there is excellent agreement between the solutions by using these two methods, when *S*=8.

In Fig. 2, three types of frequency regions[10] can be discriminated in terms of the solution of *q*: (1) Propagation region, where ql_c/π is real, and the wave propagates along the beam without attenuation. (2) Complex region, where $ql_c/\pi=\mathrm{Re}(ql_c/\pi)+\sqrt{-1}\,\mathrm{Im}(ql_c/\pi)$ with $\left|\mathrm{Im}(ql_c/\pi)\right|>0$ and $0<\left|\mathrm{Re}(ql_c/\pi)\right|<1$, and the wave propagates with attenuation. (3) Attenuation region, where $ql_c/\pi=1+\sqrt{-1}\,\mathrm{Im}(ql_c/\pi)$ with $\left|\mathrm{Im}(ql_c/\pi)\right|>0$. Such three frequency regions are labelled as P, C and A, respectively, in the central plane between Fig. 2a and Fig. 2b.

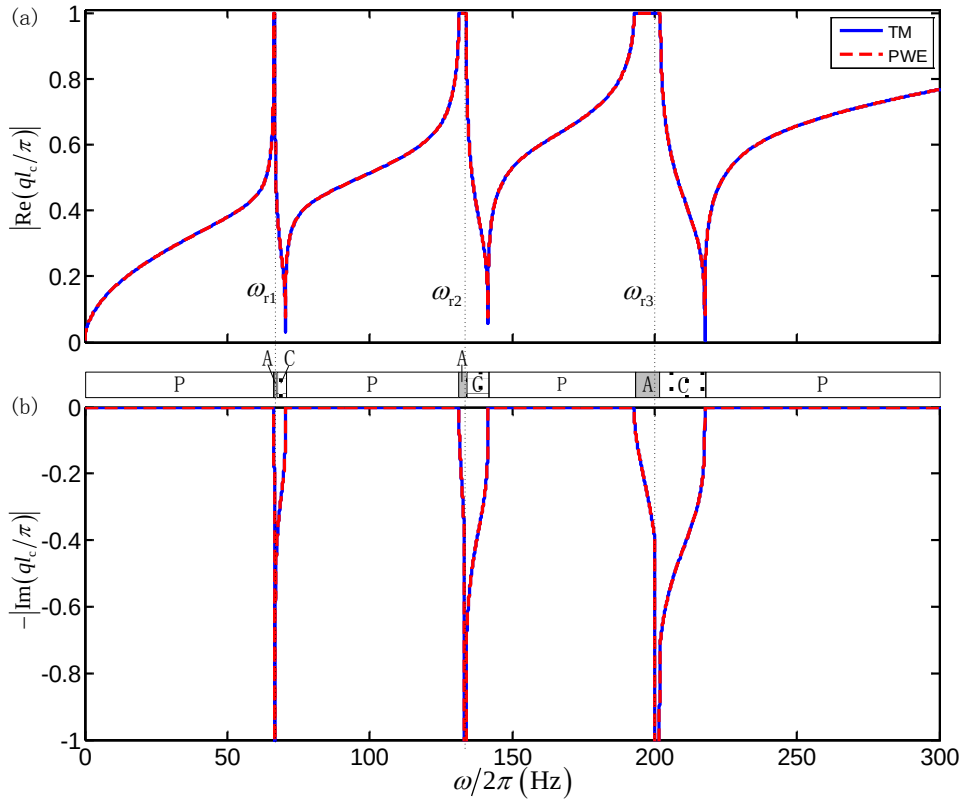

Fig. 2 Band structure of flexural wave propagation in the Euler-Bernoulli beam by using the plane wave expansion (PWE) method, which is verified the transfer matrix (TM) method. P: Propagation region, C: Complex region, A: Attenuation region.

As seen from Fig. 2, three band gaps seamlessly blending attenuation band and complex band are observed around the local resonant frequencies $\omega_{r1}/2\pi$=66.67Hz, $\omega_{r2}/2\pi$=133.33Hz, $\omega_{r2}/2\pi$=200Hz, i.e. the target frequencies. Obviously, the existence of attenuation band notably broadens the stop band of wave propagation, which could effectively improve the robustness of filtering out undesired waves, when possible uncertainties of local resonances occur. Additionally, compared with the lowest Bragg scattering frequency $\omega_{B,1}/2\pi=(\pi/l_c)^2\sqrt{EI/\rho A}/2\pi=461.77\,\mathrm{Hz}$, these band gaps should be considered as low-frequency gaps.

It is worth noting that the wave propagation within the pass bands is controlled by real wave vectors, which reflect the dispersion feature of the flexural wave freely propagating in this LR beam[10]. As shown in Fig. 2, the wave vectors within the stop bands are complex rather than real, so that there is no dispersion within the band gaps.

3.1.2 Verification of the Band gaps

When the damping χ_{b}=0.02 and χ_{r}=0.02 are taken into account, the imaginary part of the solution obtained by PWE method for this beam is depicted in Fig. 3a, which reveals the band structure. The band structure is verified by dynamic analysis for the Euler-Bernoulli beam with 10 unit cells by using the Galerkin method, as shown in Fig. 3b. As mentioned in Section 2.2, the band gaps are determined by the vibration transmittance. Negative vibration transmittances (in dB) imply wave attenuations. It is worth noting again that the actual nonlinear stiffness of the resonator rather than the linearized stiffness is used in numerical simulations.

The vibration transmittance is also obtained by finite element (FE) analysis, which is depicted in Fig. 3c. The FE model of the LR beam is shown in the inserting picture at the up-right corner of Fig. 3c. For the beam, there are 300 elements (C3D8R) along the length, and 4 elements along the thickness. The springs are modelled by the Springs/Dashpots elements, and the lengths of the oblique and vertical spring are 14.70mm and 15mm, respectively. The stiffness of the vertical spring is 2842.45N/m, and that of the oblique spring is determined according to $k_{\mathrm{o},j}$=0.5973$\left(1-\eta_j\right)k_{\mathrm{v}}$. A rigid sphere with mass 0.0018kg is used to model the lumped mass of the resonator, and rigid cuboids without mass are used to model the side supports for oblique springs. A random disturbance (white noise) acts on the left-hand end of the beam. And then the dynamic responses are achieved by using ABAQUS®/Standard.

Comparing Fig. 3a with both Fig. 3b and Fig. 3c, one can see that the band gaps revealed by the PWE method almost completely agree with those by both dynamic analysis using Galerkin method and FE analysis, which indicates that the PWE method can predict the band gaps accurately when damping is taken into account.

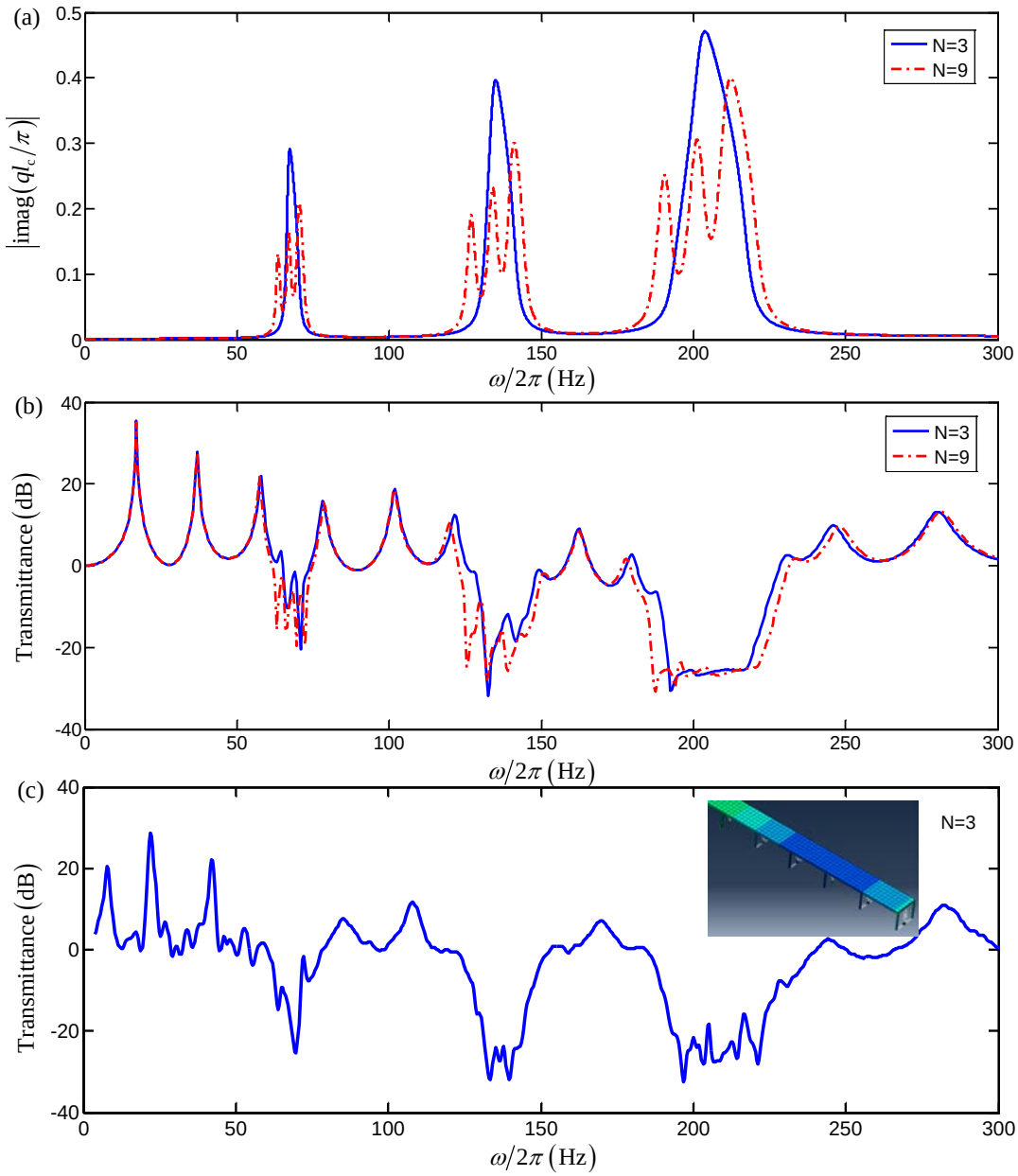

Fig. 3 Effect of adding resonators with resonant frequencies surrounding the target frequencies on broadening band gaps. (a) Image part of the solution obtained by using the PWE method. (b) Vibration transmittance of the beam calculated by using the Galerkin method. Solid lines, *N*=3; dashed-dotted lines, *N*=9. (c) Vibration transmittance by FE analysis for *N*=3; the inserting picture at the up-right corner presents the FE model of the LR beam.

3.1.3 Wave attenuation in the LR beam

Under harmonic excitations with frequencies in the Attenuation and Complex regions, the steady state responses of the LR beam with finite length (10 unit cells, 3 resonators in each unit cell) are obtained by dynamic analysis using the Galerkin

method, as shown in Fig. 4. From this figure, one can observe the deformation shapes of the beam (Fig. 4a and Fig. 4c) and resonator array (Fig. 4b and Fig. 4d), respectively. Remind that w is the transverse displacement of the beam, $w_0=w(0,t)$ is the displacement of the left-hand end of the beam, and z is the absolute displacement of the resonator.

Obviously, there is a significant spatial attenuation of the amplitude of the flexural vibration caused by the resonators. It also can be seen that most of the energy is absorbed by resonators at the beginning section of the beam, which is one of the typical features of wave attenuation by local resonance [26, 43]. Moreover, the excitation frequencies 132Hz and 136Hz are selected around the second resonant frequency 133.33Hz, so that only the second resonator in the unit cell undergoes resonance, as shown in Fig. 4b and Fig. 4d.

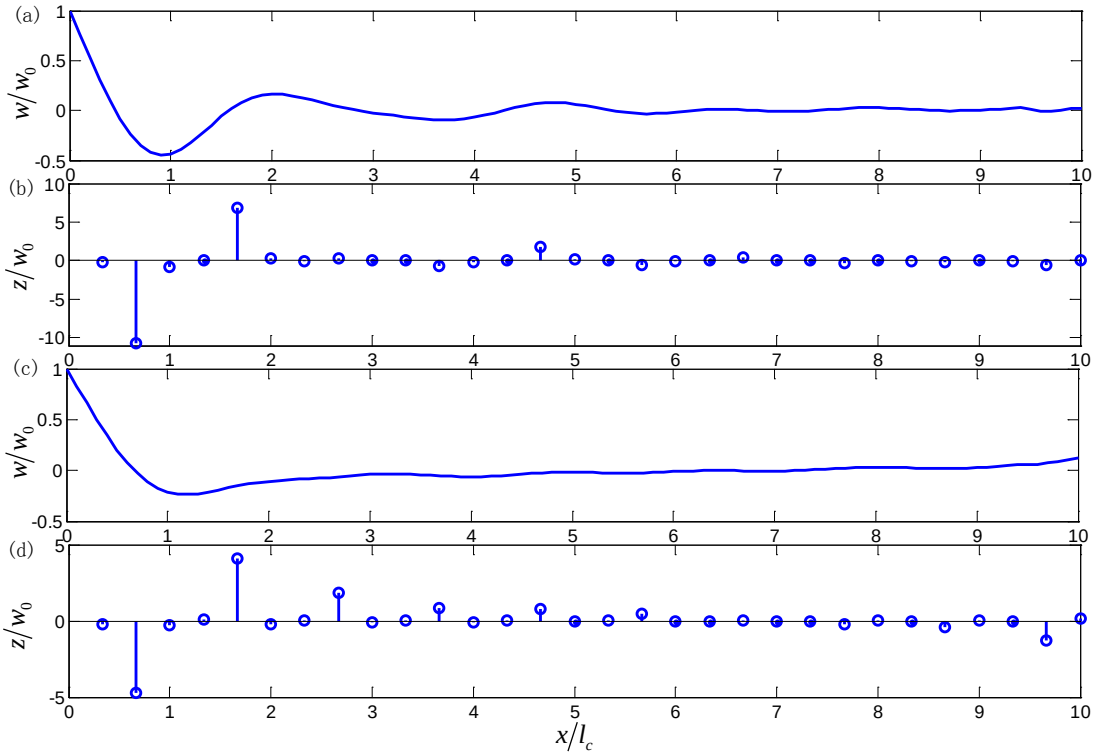

Fig. 4 Deformation shapes of the beam (a, c) and resonator array (b, d) under excitations with different frequencies: (a, b) 132Hz in Attenuation region and (c, d) 136Hz in Complex region.

3.1.4 Broadening the band gap by adding more resonators

Also shown in Fig. 2, the band gap at low frequency, such as $\omega_o/3$, is narrow. In order to further broaden this band gap, more resonators with resonant frequencies surrounding the target frequencies are added into the unit cell, as has been done by Xiao et al.[23] . For example, nine resonators are suspended onto the beam in one unit cell at equal interval with net stiffness

$$\boldsymbol{\eta} k_v = \left\{ \frac{1}{9}(1-\alpha), \frac{1}{9}, \frac{1}{9}(1+\alpha), \frac{4}{9}(1-\alpha), \frac{4}{9}, \frac{4}{9}(1+\alpha), 1-\alpha, 1, 1+\alpha \right\} k_v \qquad (21)$$

where α represents the off-set ratio of the resonant stiffness deviating from the target stiffness. Note that the mass ratio μ=0.5 remains unchanged. In other words, the mass of each resonator $m_r = \mu\rho A l_c / N$ becomes smaller as the number of resonators N increases. Moreover, one may notice that the last element of $\boldsymbol{\eta}$, i.e., $1+\alpha$, is larger than 1. In such a case, the *pre-compression* Δl should be changed into *pre-stretch* with the same magnitude to realize additional stiffness to that of the vertical spring in the vertical direction. From Fig. 3a and Fig. 3b, one can see the comparison of the band structure of the LR beam containing nine resonators in one unit cell (dash-dotted lines) with that of three resonators (solid lines), which implies that adding more resonators with natural frequencies surrounding the target frequencies has a considerable capability of broadening the band gaps.

Moreover, the degree of broadening band gaps depends on the off-set ratio α of the stiffness deviating from the target stiffness, whose effect on the band structure is depicted in Fig. 5. It can be seen that, as the off-set ratio increases, the width of the band gap become broader, but the magnitude of the peak attenuation decreases. When the off-set ratio is selected as a relatively large value, such as 0.2, each original band gap is split into three separate band gaps with narrower bandwidth, which is not expected to happen to the band structure. However, when the off-set ratio is small, such as 0.05, the band gap is hardly broadened by adding resonators, and the magnitude of imaginary part of solution is reduced, which implies that the wave

attenuation gets worse. Therefore, as a trade-off, a moderate value of α, such as 0.1 in this numerical experiment, is adopted to achieve broad and relatively-high-attenuation band gaps.

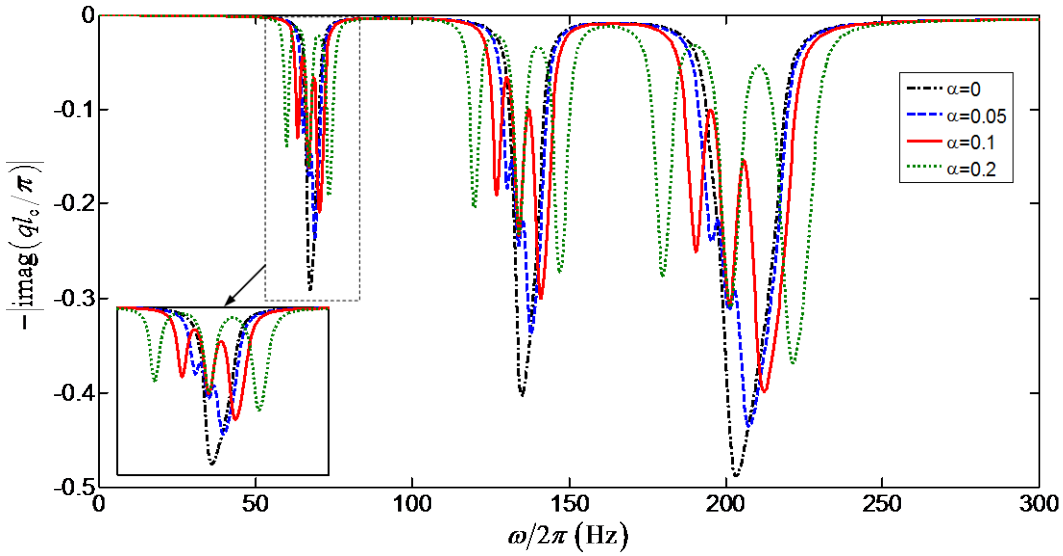

Fig. 5 Effect of the off-set ratio of the stiffness deviating from the target stiffness on the band structure. The small figure at the left bottom corner is a close-up diagram of the first band gap.

3.2 Vibration attenuation in a raft beam

This section illustrates an application of the multi-low-frequency band gap designating method in attenuating vibrations of beams in a vibration isolation floating raft[44] excited by multiple forces with different frequencies, as shown in Fig. 6. The raft beam is a No. 10 I-shape steel beam supported by two EB-400 resilient isolators at two ends, and possesses the following parameters: mass per unit length ρA=11.2 kg/m, flexural rigidity EI=5.0470×10^5 Nm^2, length L=20l_c=2m (20 unit cells). The stiffness of the resilient support is k_{rs}=1.61×10^6 N/m.

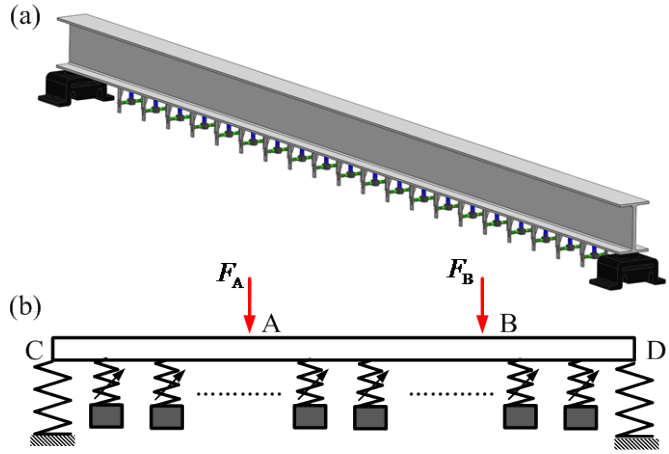

Fig. 6 (a) Schematic diagram of a raft beam with NS resonators; (b) computational model.

The wave number of this raft beam (Euler-Bernoulli beam) can be obtained from the following characteristic equation

$$\begin{aligned} & EI\beta_p^3\left(\sin\beta_p L+\sinh\beta_p L\right)-k_{\mathrm{rs}}\left(\cos\beta_p L+\cosh\beta_p L\right) \\ & -\left(EI\beta_p^3\cos\beta_p L+k_{\mathrm{rs}}\sin\beta_p L\right)\frac{2k_{\mathrm{rs}}\sinh\beta_p L+EI\beta_p^3\left(\cos\beta_p L-\cosh\beta_p L\right)}{EI\beta_p^3\left(\sinh\beta_p L-\sin\beta_p L\right)} \\ & +\left(EI\beta_p^3\cosh\beta_p L-k_{\mathrm{rs}}\sinh\beta_p L\right)\frac{2k_{\mathrm{rs}}\sinh\beta_p L+EI\beta_p^3\left(\cos\beta_p L-\cosh\beta_p L\right)}{EI\beta_p^3\left(\sinh\beta_p L-\sin\beta_p L\right)} \\ & =0 \end{aligned} \tag{22}$$

The first five natural frequencies of this raft beam supported by resilient isolators are 50.03 Hz, 101.42 Hz, 226.14 Hz, 535.39 Hz and 1028.90 Hz. The corresponding mode functions are given by

$$\begin{aligned} \phi_p\left(x\right)=&\cos\beta_p x+\cosh\beta_p x \\ &+\frac{2k_{\mathrm{rs}}\left(\sinh\beta_p L\sin\beta_p x+\sin\beta_p L\sinh\beta_p x\right)}{EI\beta_p^3\left(\sinh\beta_p L-\sin\beta_p L\right)} \\ &-\frac{\cosh\beta_p L-\cos\beta_p L}{\sinh\beta_p L-\sin\beta_p L}\left(\sin\beta_p x+\sinh\beta_p x\right) \end{aligned} \tag{23}$$

The mode functions are utilized as both the trial and weight functions for the Galerkin method to calculate the dynamic responses of the raft beam.

The excitations, acting at points A and B, have the form of

$\{F_A, F_B\} = \{F_{A0}\cos\omega_A t, F_{B0}\cos\omega_B t\}$, $\omega_A < \omega_B$. The distances between the forces and the ends are $L_{AC} = L/3$ and $L_{BD} = L/4$, respectively. In order to attenuate vibration propagation in the raft beam induced by these two excitations, two band gaps are assigned at the target frequencies ω_A and ω_B by using two resonators in a unit cell with stiffness $\left\{\left(\omega_A/\omega_B\right)^2, 1\right\}k_v$, where $k_v = m_r\omega_B^2 = \left(\mu\rho A l_c/2\right)\omega_B^2$. In this case, the mass ratio μ is still selected to be 0.5. Two excitation frequencies $\{40\text{Hz}, 110\text{Hz}\}$ are taken as an example. Since the excitation frequencies are close to the first two natural frequencies, the isolators (without the periodically distributed resonators) cannot prevent those excitations from being transmitted into the base, and the structural responses of the beam are also at high level.

Generally, the vibratory forces or power flows are expected to be prevented from being transmitted into the base, and hence the receptances at the two ends of the beam are considered here to evaluate the performance of wave attenuation. The band gaps of these receptances at the target frequencies are created to attenuate undesired vibrations transmitted into the base through isolators supporting the raft beam.

The receptances R_{ij} of the raft beam is defined as the displacement at the *j*th point induced by a unit force acting at the *i*th point on the beam. For the raft beam coupled with two resonators in each unit cell, the receptances R_{BC} and R_{BD} calculated by dynamic analysis (DA) using Galerkin method are presented in decibel $20\log_{10}\left(R_{ij}/1\times10^{-6}\right)$ in Fig. 7, which are validated by FE analysis (FEA). Such an FE analysis is carried out by using the commercial FE package ABAQUS® again. The modelling procedure of the raft beam coupled with resonators is similar to that of the LR-beam in Section 3.1. It should be noted that the resilient support of the raft beam is modelled as a Springs/Dashpots element with stiffness k_{rs}, due to a lack of knowledge of material parameters of the resilient support (rubber). As seen from Fig.

7, generally, the band structure of receptances revealed by dynamics analysis using Galerkin method agrees well with that predicated by FE analysis.

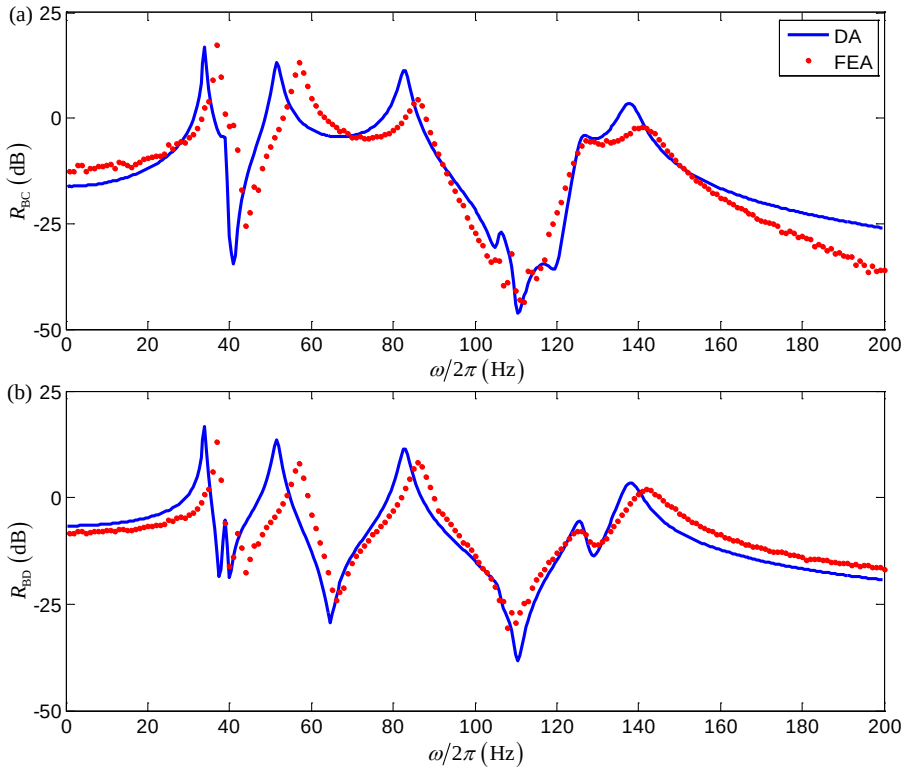

Fig.7 Receptances of the raft beam with two resonators in each unit cell. (a) R_{BC}, (b) R_{BD}. Solid lines represent the receptances obtained by dynamic analysis (DA) using Galerkin method, and dotes denote finite element analysis (FEA).

Furthermore, the receptances at two ends of the raft beam are compared with those of a bare beam (without resonators), as shown in Fig. 8. Obviously, there are two gaps of receptances at the target frequencies (dashed-dotted lines), which imply that the vibrations at the frequencies in the vicinity of the target frequencies can be sufficiently attenuated by the periodic beam with resonators. The bandwidth at the higher frequency is broader than that at the lower one, due to the fact that the bandwidth of a LR band gap is in proportion to the magnitude of the resonant frequency. By comparing Fig. 8a with Fig. 8b, and Fig. 8c with Fig. 8d, one can see that the attenuation performances of R_{AD} and R_{BC} are better than R_{AC} and R_{BD}, respectively, at both the two target frequencies, because the distances L_{AD} and L_{BC} are larger than L_{AC} and L_{BD}, respectively, which implies that the farther the point of

collecting responses is away from the point of acting force, the better attenuation performance is obtained. This can be attributed to the fact that sufficient resonators are required to achieve good attenuations.

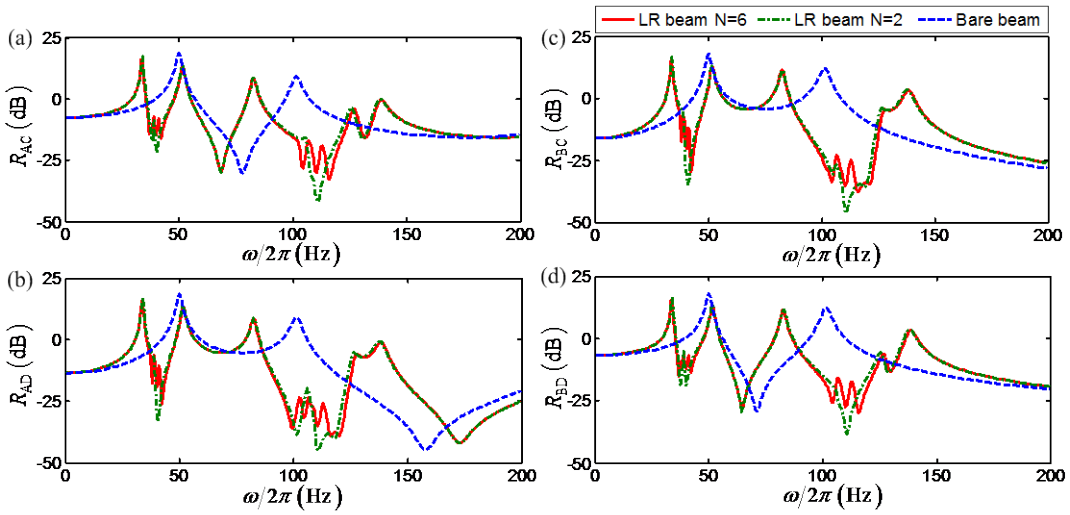

Fig.8 Receptances of the raft beam with and without resonators. (a) R_{AC}, (b) R_{AD}, (c) R_{BC}, (d) R_{BD}. Solid lines represent the receptances of the raft beam with 6 resonators in one unit cell, dashed-dotted lines 2 resonators, and dashed lines the bare beam without resonators.

It also can be seen from Fig. 8 that the band gaps are narrow at the target frequency ω_A, especially for R_{AD} and R_{BC}, where sharp dips are observed. In order to broaden these band gaps, more resonators with resonant frequencies surrounding the target frequencies are added into the unit cell. The corresponding stiffness array of the resonators is given by

$$\boldsymbol{\eta} k_v = \left\{ \left(\frac{\omega_A}{\omega_B}\right)^2 (1-\alpha), \left(\frac{\omega_A}{\omega_B}\right)^2, \left(\frac{\omega_A}{\omega_B}\right)^2 (1+\alpha), 1-\alpha, 1, 1+\alpha \right\} k_v \tag{24}$$

where the off-set ratio α is selected as 0.1 again and the mass ratio μ=0.5 remains unchanged. After more resonators are added onto the raft beam, the receptances are depicted as solid lines in Fig. 8. One can see that the band gaps are broadened by adding resonators, which could improve the robustness of this method to deal with possible uncertainties of the stiffness of the resonators and possible shifts of the excitation frequencies from the target frequencies, although peak attenuations in the

band gaps would be reduced to some extent.

4. Conclusions

Multi-low-frequency band gaps of flexural wave in beams are assigned by using local resonators containing negative-stiffness (NS) mechanisms. The mass of the resonator is suspended by a vertical spring connecting with two oblique springs, which act as an NS mechanism and can reduce the stiffness of the resonator to a desired value. Numerical experiments are carried out to verify the proposed method, and the results reveal that multiple band gaps at low target frequencies can be opened using multiple resonators in one unit cell, and a stop band seamlessly blending attenuation band and complex band is observed, which notably broaden the band gaps.

It is also found that adding more resonators into the unit cell can effectively broaden the band gaps, when their resonant frequencies surrounds the target frequencies with a proper off-set ratio (defined as frequency deviation from the target frequency divided by the target frequency). Additionally, an engineering application of the proposed method for attenuating flexural vibrations in a raft beam excited by two forces with different low frequencies is demonstrated, which indicates that the multi-low-frequency flexural vibrations can be effectively attenuated through assigning band gaps of receptances at the target frequencies.

Acknowledgements

This research work was supported by National Natural Science Foundation of China (11572116), Natural Science Foundation of Hunan Province (2016JJ3036), and Fundamental Research Funds for the Central Universities. This work is carried out during the first author’s visit to the University of Liverpool.

Declarations of interest

The authors declare no conflict of interest.

References

1. L. Brillouin, *Wave Propagation in Periodic Structures: Electric Filters and Crystal Lattices*. (Dover Publications, Inc., New York, 1946).
2. Z. Liu, X. Zhang, Y. Mao, Y. Y. Zhu, Z. Yang, C. T. Chan and P. Sheng, Science **289** (5485), 1734-1736 (2000).
3. O. Sigmund and J. Søndergaard Jensen, Philosophical Transactions of the Royal Society of London. Series A: Mathematical, Physical and Engineering Sciences **361** (1806), 1001-1019 (2003).
4. J. Wen, G. Wang, D. Yu, H. Zhao and Y. Liu, Journal of Applied Physics **97** (11), 114907 (2005).
5. M. I. Hussein, K. Hamza, G. M. Hulbert and K. Saitou, Waves in Random and Complex Media **17** (4), 491-510 (2007).
6. Y. Yang, A. S. Fallah and L. A. Louca, Journal of Sound and Vibration **327** (1–2), 26-40 (2009).
7. H. J. Xiang, Z. F. Shi, S. J. Wang and Y. L. Mo, Smart Materials and Structures **21** (11), 112003 (2012).
8. M. I. Hussein, M. J. Leamy and M. Ruzzene, Applied Mechanics Reviews **66** (4), 040802-040802 (2014).
9. D. Yu, Y. Liu, G. Wang, H. Zhao and J. Qiu, Journal of Applied Physics **100** (12), 124901 (2006).
10. Y. Xiao, J. Wen, D. Yu and X. Wen, Journal of Sound and Vibration **332** (4), 867-893 (2013).
11. M. Oudich, Y. Li, B. M. Assouar and Z. Hou, New Journal of Physics **12** (8), 083049 (2010).
12. C. Goffaux and J. Sánchez-Dehesa, Physical Review B **67** (14), 144301 (2003).
13. C. Yilmaz, G. M. Hulbert and N. Kikuchi, Physical Review B **76** (5), 054309 (2007).
14. C. Yilmaz and G. M. Hulbert, Physics Letters A **374** (34), 3576-3584 (2010).
15. G. Acar and C. Yilmaz, Journal of Sound and Vibration **332** (24), 6389-6404 (2013).
16. N. M. M. Frandsen, O. R. Bilal, J. S. Jensen and M. I. Hussein, Journal of Applied Physics **119** (12), 124902 (2016).
17. O. R. Bilal and M. I. Hussein, Applied Physics Letters **103** (11), 111901 (2013).
18. M. Badreddine Assouar, J.-H. Sun, F.-S. Lin and J.-C. Hsu, Ultrasonics **54** (8), 2159-2164 (2014).
19. J. Zhou, K. Wang, D. Xu and H. Ouyang, Journal of Applied Physics **121** (4), 044902 (2017).
20. T. L. Smith, K. Rao and I. Dyer, Noise Control Engineering Journal **26**, 56-60 (1986).
21. M. Y. Wang, Y. T. Choy, C. W. Wan and A. S. Zhao, Journal of Vibration and Acoustics **137** (6), 064504-064504 (2015).
22. X. Wang and M. Y. Wang, Meccanica **51** (1), 171-178 (2016).

23. Y. Xiao, J. Wen and X. Wen, Physics Letters A **376** (16), 1384-1390 (2012).
24. K. L. Tsakmakidis, A. D. Boardman and O. Hess, Nature **450** (7168), 397-401 (2007).
25. J. Zhu, Y. Chen, X. Zhu, F. J. Garcia-Vidal, X. Yin, W. Zhang and X. Zhang, Scientific Reports **3**, 1728 (2013).
26. S. Krödel, N. Thomé and C. Daraio, Extreme Mechanics Letters **4**, 111-117 (2015).
27. P. Zhang, Z. Wang, Y. Zhang and X. Liang, Science China Physics, Mechanics and Astronomy **56** (7), 1253-1262 (2013).
28. T. Wang, M.-P. Sheng and Q.-H. Qin, Physics Letters A **380** (4), 525-529 (2016).
29. P. F. Pai, H. Peng and S. Jiang, International Journal of Mechanical Sciences **79**, 195-205 (2014).
30. Q. Cao, M. Wiercigroch, Pavlovskaia, E. E, C. Grebogi, T. Thompson and J. Michael, Physical Review E **74** (4), 046218 (2006).
31. M. M. Sigalas and C. M. Soukoulis, Physical Review B **51** (5), 2780-2789 (1995).
32. Z. Hou, W. Kuang and Y. Liu, Physics Letters A **333** (1), 172-180 (2004).
33. F. Romeo and A. Luongo, Journal of Sound and Vibration **268** (3), 601-615 (2003).
34. D. Yu, Y. Liu, H. Zhao, G. Wang and J. Qiu, Physical Review B **73** (6), 064301 (2006).
35. L. Liu and M. I. Hussein, Journal of Applied Mechanics **79** (1), 011003 (2011).
36. R. Zhu, X. N. Liu, G. K. Hu, C. T. Sun and G. L. Huang, Journal of Sound and Vibration **333** (10), 2759-2773 (2014).
37. M. M. Sigalas and E. N. Economou, Journal of Sound and Vibration **158** (2), 377-382 (1992).
38. M. S. Kushwaha, P. Halevi, L. Dobrzynski and B. Djafari-Rouhani, Physical Review Letters **71** (13), 2022-2025 (1993).
39. S. Xiao, L. Shen and S. He, Physics Letters A **313** (1), 132-138 (2003).
40. Y. Cao, Z. Hou and Y. Liu, Physics Letters A **327** (2), 247-253 (2004).
41. Z. Hou and B. M. Assouar, Physics Letters A **372** (12), 2091-2097 (2008).
42. V. Romero-García, J. V. Sánchez-Pérez and L. M. Garcia-Raffi, Journal of Applied Physics **108** (4), 044907 (2010).
43. J. S. Chen, B. Sharma and C. T. Sun, Composite Structures **93** (8), 2120-2125 (2011).
44. T. Yang, Y. Sun, L. Zhou, M. J. Brennan and Z. Liu, Case Studies in Mechanical Systems and Signal Processing **1**, 32-37 (2015).